JACS
JOURNAL OF THE AMERICAN CHEMICAL SOCIETY
pubs.acs.org/JACS
Article

Field-Responsive Dynamic Monolayer Regulated Interphase for Enhanced Lithium Metal Batteries

Elizabeth Zhang, John Holoubek, Hao Lyu, Yuqi Li, Jacob Florian, Sanzeeda Baig Shuchi, Jane K.J. Lee, Lukas Michalek, Tianyang Chen, Zhouyi Chen, Il Rok Choi, Xuelin Guo, Luca Mondonico, Yi Cui,* and Zhenan Bao*

Cite This: J. Am. Chem. Soc. 2026, 148, 6365–6378

ABSTRACT: Lithium metal batteries offer high energy density but suffer from persistent interphase instability, where continuous corrosion, solid electrolyte interphase (SEI) growth and poor lithium deposition morphology remain key barriers to long cycle and calendar life. Here, we introduce a novel concept of dynamic monolayers on Li metal anodes, consisting of electric field-responsive molecules that assemble into packed, structured layers at the lithium interphase under an applied voltage. We employed electrochemical quartz crystal microbalance with dissipation monitoring for in situ verification of the field responsiveness and packing behavior of these molecules. Dynamic monolayers with stronger packing are found to promote more inorganic-rich SEI and chunkier lithium growth, as directly observed by cryogenic X-ray photoelectron spectroscopy and *operando* optical microscopy. Together, these interfacial improvements translate into enhanced Coulombic Efficiency, reduced overpotential, and improved long-term cycling stability across Li||Cu, Li||Li, ultrathin lithium (20 μm) and anode-free NMC811 configurations. Dynamic monolayers potentially provide a broadly applicable approach for tackling interfacial challenges across a range of alkali metal battery systems.

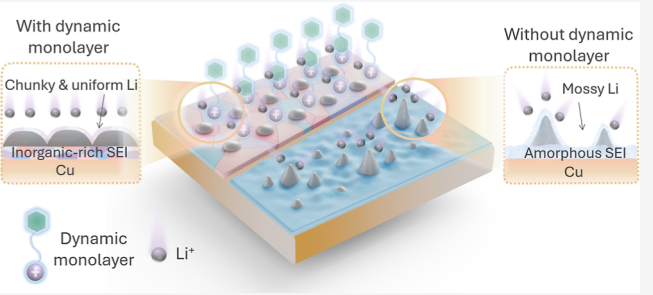

INTRODUCTION

Lithium metal is widely regarded as a promising anode material for next-generation energy storage, owing to its high theoretical specific capacity and the lowest electrochemical potential among known materials.[1−3] These properties enable lithium metal batteries (LMBs) the potential for much higher energy density compared to conventional lithium-ion systems, making them attractive for applications such as electric vehicles.[1] However, their practical deployment has been hindered by persistent interfacial instability.[4] The root of these challenges lies in the intrinsic reactivity of lithium metal with conventional electrolytes, which leads to the continuous formation and growth of a solid electrolyte interphase (SEI). This ongoing SEI regeneration consumes both lithium and electrolyte, reducing the amount of active lithium and diminishing cyclable capacity.[5] In parallel, lithium tends to deposit in nonuniform, whisker-like morphologies during cycling.[6] These mossy structures increase the risk of dendrite formation and contribute to the buildup of dead lithium—electrically isolated lithium that cannot participate in further cycling.[7,8] Together, uncontrolled SEI growth and dead lithium accumulation significantly degrade cycle life, calendar life, and Coulombic efficiency (CE).[9]

To combat these interphase-related issues, a variety of strategies have been explored. These include the design of new electrolyte formulations,[10−15] polymer coatings,[16−18] and the use of functional additives with tailored roles.[19−22] Among the many strategies explored to address lithium metal battery challenges, it is particularly important to develop approaches that simultaneously regulate lithium deposition and promote stable SEI formation. One of the key contributors to poor deposition morphology is uneven lithium ion flux, where certain regions on the electrode surface experience higher current densities and accelerate dendritic growth. To mitigate this issue, electric-field-responsive cationic additives[23−27] have been introduced to redistribute lithium-ion flux and promote smoother deposition. While effective in modulating morphology, they often lack controlled interfacial organization and do not necessarily enhance SEI stability.

On the other end of the spectrum, self-assembled monolayers (SAMs) have also been employed in LMBs as highly ordered molecular assemblies that can be tailored to improve cell performance.[28,29] Here, the ability of molecules to

Received: November 1, 2025
Revised: January 27, 2026
Accepted: January 29, 2026
Published: February 6, 2026

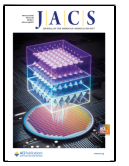

https://doi.org/10.1021/jacs.5c19365
J. Am. Chem. Soc. 2026, 148, 6365−6378

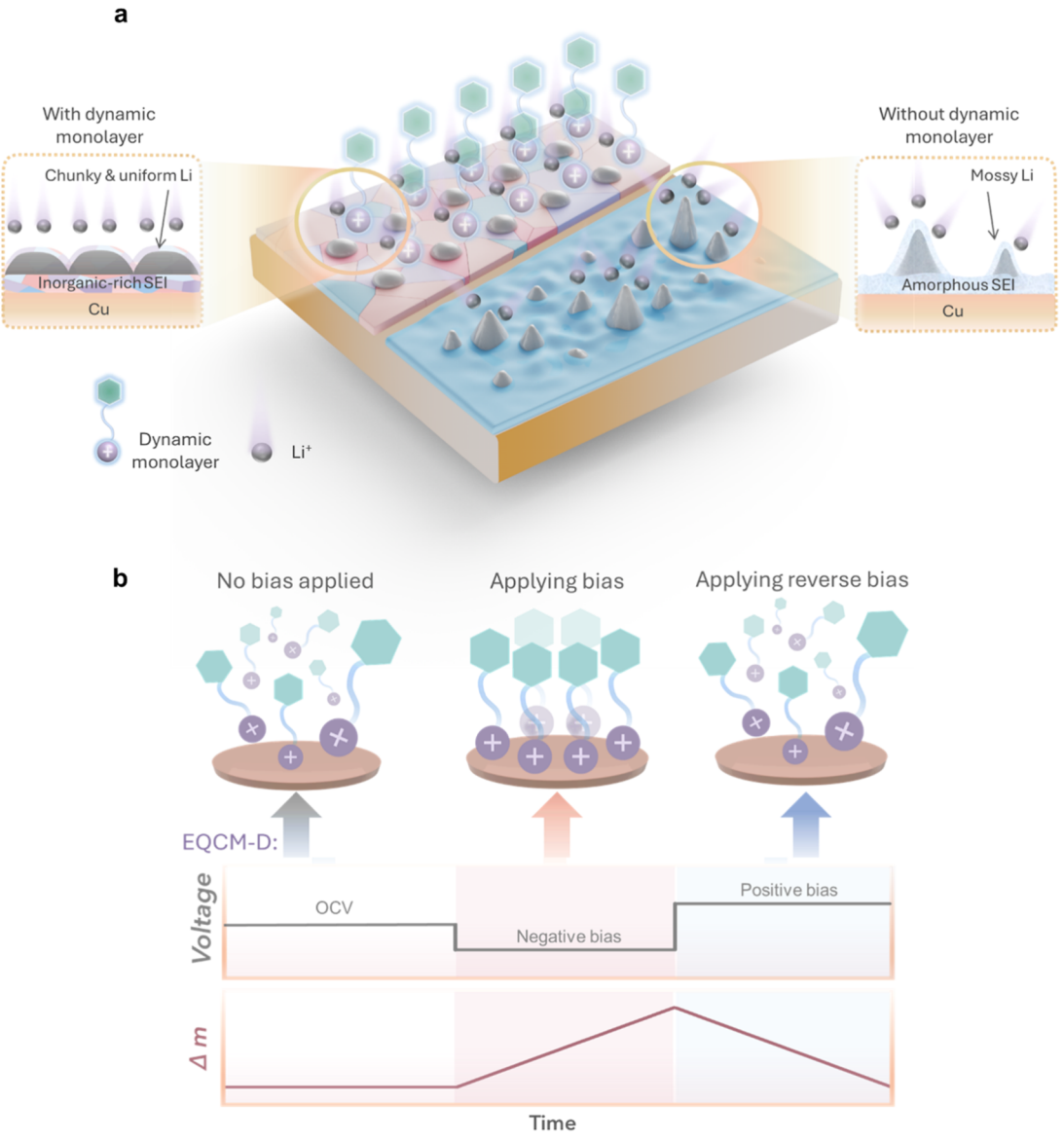

Figure 1. (a) Schematic summarizing the effects of the dynamic monolayer. More inorganic solid electrolyte interphase formation and more uniform lithium deposition are illustrated. (b) Schematic showing the field-responsive nature of the dynamic monolayer. When no bias is applied, the dynamic monolayers are dispersed in the electrolyte (no mass detected at the electrode). When a negative bias is applied, the dynamic monolayers assemble at the interphase in an ordered fashion (increase in mass detected at the electrode). When a positive bias is applied, the dynamic monolayer is repelled away from the interphase (decrease in mass detected at the electrode).

pack in an ordered fashion offers significant benefits. However, a key limitation is that these molecules are chemically anchored to the surface, preventing their removal or reconfiguration under operating conditions. Their inability to respond to electric field prevents them from adapting to changes in local potential or ion flux during cycling, limiting their capacity to dynamically regulate lithium deposition or accommodate interphase evolution.

In principle, a monolayer capable of reversible assembly and disassembly in response to the electric field would represent an ideal interphase design: (i) adapting dynamic responsiveness to local lithium-ion flux, allowing real-time adjustment of surface coverage, and (ii) forming an ordered interfacial layer that not only guides lithium flux but also selectively recruits favorable SEI-forming species. Such a system could actively regulate interfacial reactions and lithium deposition morphology during cycling, in contrast to fixed monolayers that cannot adapt once formed and fully disordered molecular additives that lack structural guidance. Notably, a recent study in zinc aqueous battery systems reported that macroscopic ordering at the interphase led to liquid crystal formation, which significantly improved zinc deposition morphology.[30] To our knowledge, there have been no studies investigating molecular systems capable of forming such ordered yet field-responsive assemblies at the lithium−electrolyte interphase.

In this work, we introduce a new class of field-responsive interphase modifier designed to reversibly adsorb and desorb in response to electric fields, forming a "dynamic monolayer" at the lithium metal surface. Our approach enables field-responsive organization that assembles and disassembles in situ, as monitored by electrochemical quartz crystal microbalance with dissipation monitoring (EQCM-D). As shown in Figure 1b, applying a negative bias on Li metal drives the dynamic monolayer molecules with positively charge head

https://doi.org/10.1021/jacs.5c19365
J. Am. Chem. Soc. 2026, 148, 6365−6378

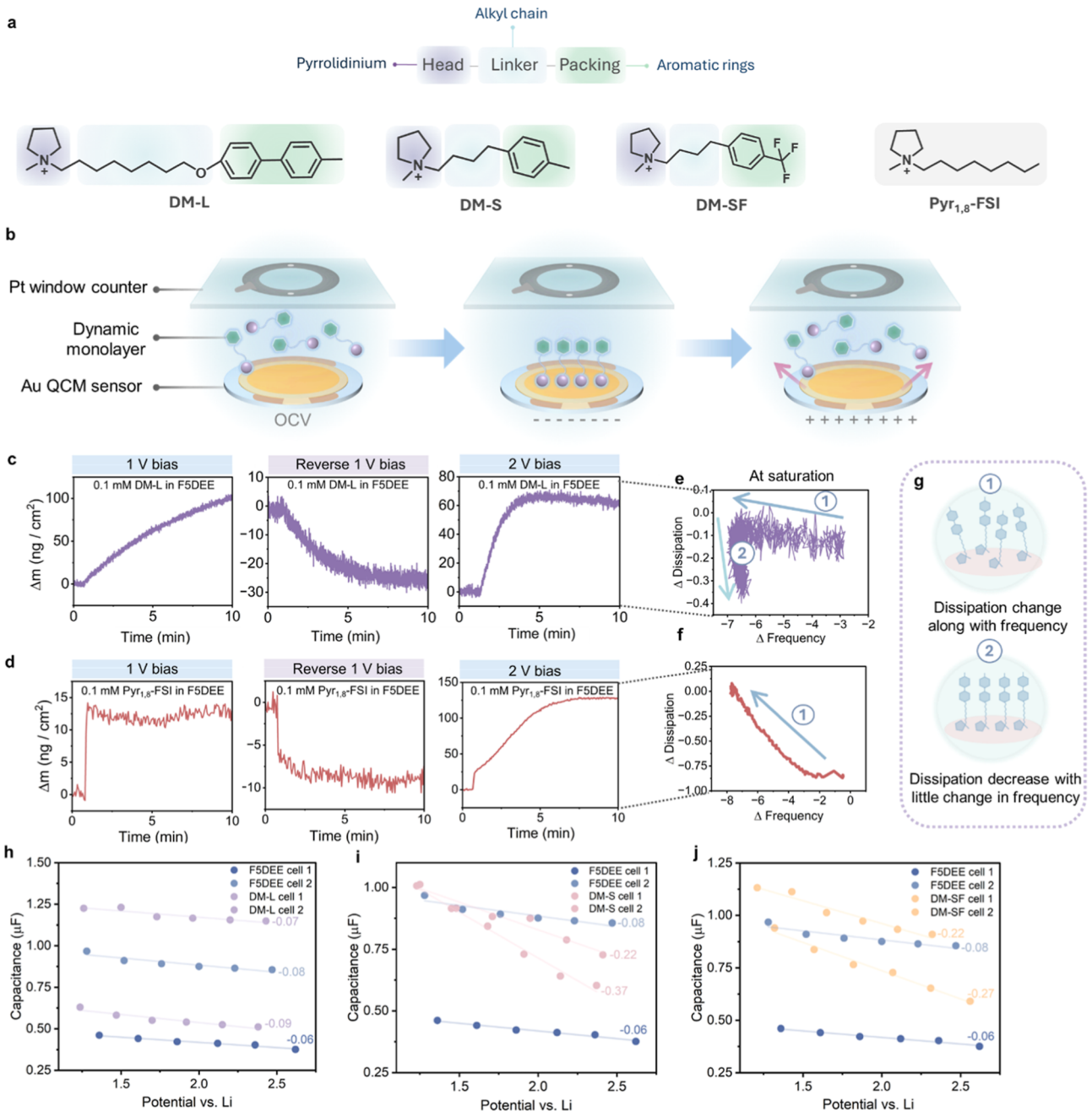

Figure 2. (a) Molecular design principle of the three types of dynamic monolayers. The dynamic monolayer generally consists of a headgroup that is stable at lithium potential, a linker, and packing unit. (b) Schematic demonstrating how electrochemical quartz crystal microbalance with dissipation monitoring is employed to detect dynamic monolayer adsorption and desorption when electric field is applied. (c,d) Change in mass over time recorded with EQCM-D for (c) 0.1 mM DM-L in F5DEE and (d) 0.1 mM $Pry_{1,8}$-FSI in F5DEE. (e,f) The Δ dissipation vs Δ frequency at saturation for DM-L and $Pry_{1,8}$-FSI. Significant decrease in dissipation is observed at saturation for DM-L compared to $Pry_{1,8}$-FSI. (g) Schematic illustrating the two processes observed with the Δ dissipation vs Δ frequency plot. (h–j) SPEIS measurement achieved with 3-electrode cells for 1.2 M LiFSI/F5DEE compared with (h) 0.1 mM DM-L in 1.2 M LiFSI/F5DEE (i) 0.1 mM DM-S in 1.2 M LiFSI/F5DEE (j) 0.1 mM DM-SF in 1.2 M LiFSI/F5DEE.

groups toward the surface, where they organize into a packed assembly. The ordered packing of these molecules recruits bis(fluorosulfonyl)imide (FSI^-) anions, promoting more inorganic-rich SEI formation. Simultaneously, the molecular arrangement provides directional guidance for lithium-ion transport, contributing to smoother and more uniform deposition. The key advantages of the dynamic monolayer are summarized in Figure 1a.

RESULTS AND DISCUSSION

Designing Field-Responsive Dynamic Monolayer for Interphase Control

We designed and synthesized a variety of dynamic monolayer molecules (see Figures S1–S6 for characterization details), which all contain three essential components (head, linker, and packing units) (Figure 2a). Each component was carefully

https://doi.org/10.1021/jacs.5c19365
J. Am. Chem. Soc. 2026, 148, 6365–6378

designed to produce varied responses to the electric field and to modulate molecular packing at the interphase.

We selected pyrrolidinium as the headgroup due to its previously reported compatibility with lithium metal anodes.[31] This stability is crucial for enabling stable dynamic behaviors at the electrode surface under highly reducing conditions. The linker unit, consisting of alkyl chains with varying length, provides molecular flexibility and facilitates the interfacial alignment.[32] The different chain lengths can potentially lead to different responses to electric field, as well as influencing the packing properties.

A key feature of the dynamic monolayer is the packing unit, which enables field-induced ordering at the interphase. To investigate how molecular structure affects this ordering, we varied (1) number of aromatic units (2) structure of the aromatic units. Aromatic groups are known to participate in $\pi-\pi$ interactions, which drive ordered molecular assembly.[33] The number of aromatic units directly impacts the packing strength:[34] the increased number of rings in DM-L compared to DM-S is expected to enhance intermolecular interactions and promote more robust assembly. To further disrupt packing, we introduce CF_3 group in DM-SF. This introduces steric hindrance and increases intermolecular spacing, thereby weakening close packing.[36] In addition, fluorine atoms may form weak hydrogen bonds that compete with $\pi-\pi$ stacking, further altering the packing behavior. The CF_3 substitution can also increase solvent-phobicity, which helps reduce solvent presence near the interphase and can potentially suppress solvent decomposition.[35]

In our study, $Pyr_{1,8}$-FSI represents the control molecule without a packing unit, providing a direct probe for the role of ordered assembly in interfacial behavior and electrochemical performance.

Probing Electric Field-Induced Assembly Behavior

To study the field-responsive behavior of dynamic monolayers, we employed electrochemical quartz crystal microbalance with dissipation monitoring (EQCM-D) as the primary characterization technique. EQCM-D detects mass changes on an electrode surface by measuring shifts in the resonance frequency of a quartz crystal. According to the Sauerbrey equation (Figure S10),[38,39] frequency is inversely proportional to mass. This technique thus enables real-time tracking of adsorption and desorption processes.[37,52] With its high sensitivity, EQCM-D can detect changes in mass down to the nanogram level. In addition to mass, EQCM-D also provides information on the mechanical properties of the interfacial layer by analyzing the relationship between frequency change and energy dissipation.[37,39] A schematic illustration of the EQCM-D working mechanism is shown in Figure 2b. The EQCM-D setup includes a gold-coated quartz crystal as the working electrode and a platinum window as the counter electrode.

At open-circuit voltage (OCV), the dynamic monolayer molecules were dispersed in the bulk electrolyte. Upon application of a negative bias, the gold surface becomes more negatively charged, attracting positively charged molecules to the electrode surface. These molecules assemble at the interphase in an ordered fashion. When the electric field is reversed, the molecules desorb and return to the bulk electrolyte. This reversible process was captured in the Δ mass vs time plots shown in Figure 2c,d. Figure 2c shows the response of a system with 0.1 mM DM-L in F5DEE, while Figure 2d shows 0.1 mM $Pyr_{1,8}$-FSI in the same solvent. Note that F5DEE[10] is a fluorinated ether that has been demonstrated to show good performance in lithium metal battery systems, the details of which are described in Figure S7. No LiFSI salt was added in either case. The original frequency vs time data is shown in Figures S11−S13, and average frequency values were used to calculate mass (in $ng \cdot cm^{-2}$) using the Sauerbrey equation (Figure S10).[38,39] The validity of Sauerbrey equation for our system is discussed in more detail in Supporting Information Note 2.

In both systems, the electrode was held at OCV until a stable baseline was reached, after which a +1 V bias (vs OCV) was applied for 10 min. As soon as the field was applied, negative charges accumulated at the gold sensor surface, attracting cationic species and leading to an increase in detected mass. In the DM-L system, over 100 $ng \cdot cm^{-2}$ of mass increase was observed during this period, whereas in the $Pyr_{1,8}$-FSI system, only ∼20 $ng \cdot cm^{-2}$ was detected. This variation may be partially attributed to the higher molecular weight of DM-L compared to $Pyr_{1,8}$-FSI, as DM-L is approximately 164 $g \cdot mol^{-1}$ heavier than $Pyr_{1,8}$-FSI. However, another likely explanation is anion decomposition. As will be discussed in later sections, DM-L appears to recruit more anions (FSI^-) to the interphase, promoting more anion decomposition. Since all cations in these systems are paired with FSI^- counterions, the mass increase detected in EQCM-D may also reflect contributions from FSI^- breakdown products. This is further supported by the behavior observed during the application of a reverse bias. In the $Pyr_{1,8}$-FSI system, the mass change was fully reversible, consistent with purely field-responsive adsorption and desorption. In contrast, in the DM-L system, a portion of the accumulated mass remained at the interphase even after applying a reverse 1 V bias, indicating that some of the mass uptake is not field-responsive and is likely due to irreversible anion decomposition. Additional analysis of the frequency and mass changes, along with the estimated number of adsorbed molecules per nm^2, is provided in the Supporting Information (Figures S11−S13). These calculations were performed under clearly stated assumptions stated in the Supporting Information for each system (Supporting Infomation Tables S1−S3 and Supporting Infomation Note 1).

To further examine monolayer behavior at potentials closer to lithium plating, we applied a +2 V bias (vs OCV) to both DM-L and $Pyr_{1,8}$-FSI systems for 10 min. In both cases, the mass initially increased and then plateaued, indicating a saturation behavior where the electrode surface becomes fully covered with adsorbed molecules. At this point, no additional charged species can be accommodated. Notably, $Pyr_{1,8}$-FSI showed a higher number of molecules adsorbed at saturation compared to DM-L, potentially due to its smaller size (Supporting Information Tables S1 and S2).

To probe the nature of the interphase formed at saturation, we analyzed the dissipation vs frequency change throughout the 2 V bias period (Figure 2e,f). As explained in Figure 2g, two distinct processes were observed. Initially, both systems exhibit a decrease in frequency accompanied by an increase in dissipation—typical behavior for molecular adsorption. However, the second stage differs between the two systems. In the DM-L system, we observe a sharp decrease in dissipation with minimal change in frequency. This pattern is characteristic of the formation of a rigid, densely packed layer, as reduced dissipation reflects less energy loss during oscillation, which occurs when the interfacial layer is mechanically stiff and well-

https://doi.org/10.1021/jacs.5c19365
J. Am. Chem. Soc. 2026, 148, 6365−6378

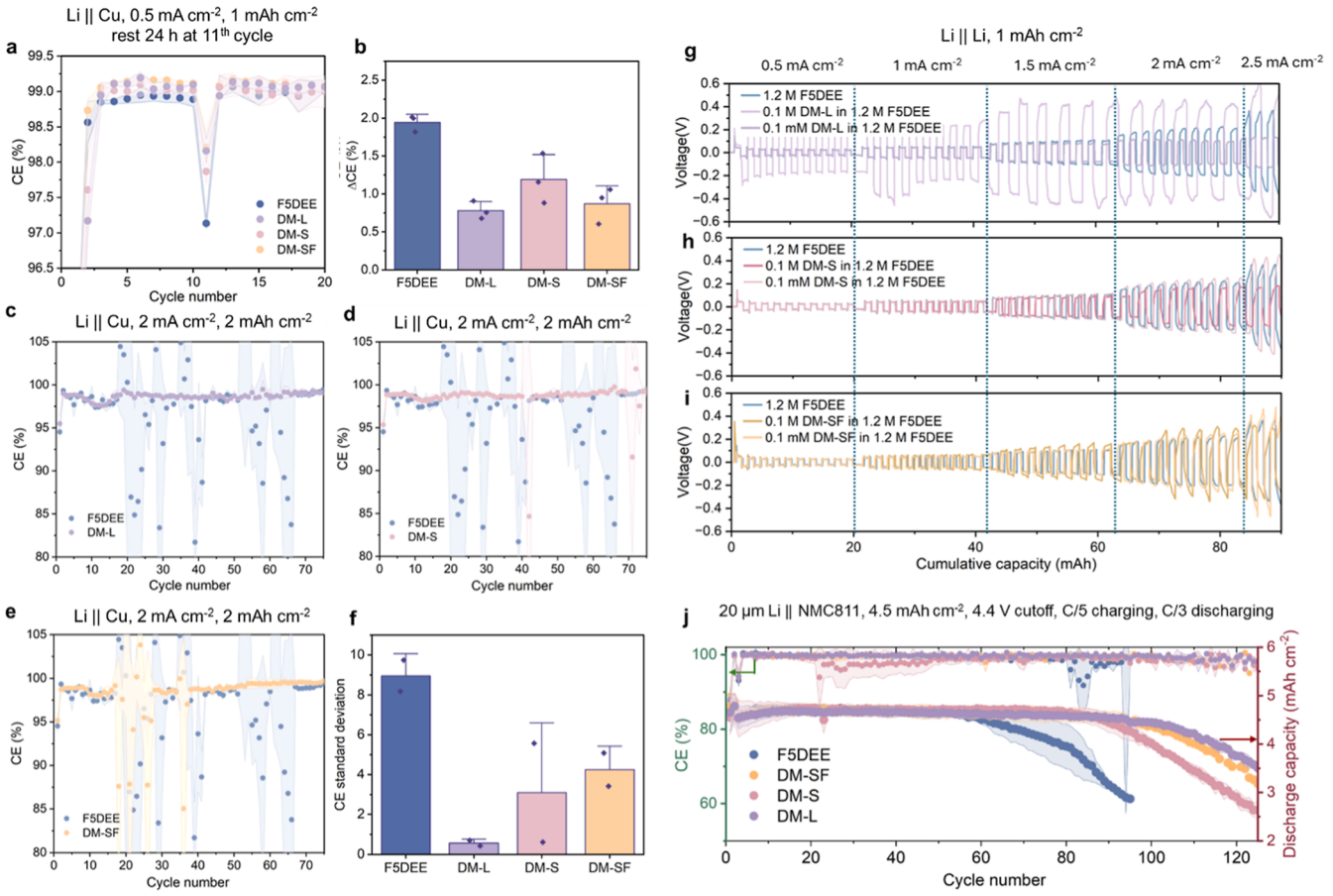

Figure 3. For all coin cell performance data, 0.1 mM of dynamic monolayer is added to 1.2 M LiFSI/F5DEE. (a) Calendar aging experiment carried out in Li||Cu half cells. The cells were cycled at 0.5 mA cm^{-2} and 1 mAh cm^{-2} for 10 cycles before resting for 24 h at plated state. The cells go back to continuous cycling after the 24 h rest. (b) The ΔCE for all four systems showing reduced corrosion with dynamic monolayer addition. There is over 50% reduction in ΔCE for DM-L. (c–e) Li||Cu half cell cycling at 2 mA cm^{-2} and 2 mAh cm^{-2} for all three dynamic monolayer systems compared to 1.2 M LiFSI/F5DEE. (f) The standard deviation in CE for 1.2 M LiFSI/F5DEE compared with the three dynamic monolayer systems. Significant fluctuation in CE is observed in electrolyte without dynamic monolayer. (g–i) Li||Li symmetric cells cycling with varying current densities, ranging from 0.5 mA cm^{-2} to 2.5 mA cm^{-2}. Two concentrations of dynamic monolayer addition (0.1 M and 0.1 mM) are compared with 1.2 M LiFSI/F5DEE. Significant change in overpotential was observed with DM-L addition. (j) 20 μm||NMC811 coin cell cycling for all four electrolytes. The cells were cycled at C/5 charging and C/3 discharging (4.5 mAh cm^{-2} cathode loading) condition with 4.4 V cutoff. Improved capacity retention was observed with the addition of dynamic monolayer.

structured.[37] In contrast, the $Pyr_{1,8}$-FSI system does not show a significant dissipation change during saturation, suggesting a less ordered, softer interfacial structure.

To further validate that the retained mass observed in the DM-L system is due to FSI^- decomposition, FSI^- was replaced with Br^- as the counterion and the study was repeated under identical conditions. Since Br^- is not expected to decompose under these conditions, any mass retained upon removing the electric field should correspond to physically adsorbed species. The frequency and mass vs time data for this Br^- system are shown in Figures S13–S15. Unlike FSI^-, Br^- can slowly adsorb to the gold surface over time,[40] resulting in a slightly increasing baseline before the field is applied. Once the bias was turned on, Br^- ions were first repelled from the surface, followed by the adsorption of DM-L. Upon removal of the electric field, Br^- returned to the surface, and the mass gradually decreases, indicating that DM-L molecules can also leave the interphase over time, even without applying a reverse bias. This reversibility supports the conclusion that the irreversible mass increase observed with FSI^- is primarily due to anion decomposition, not incomplete desorption of DM-L. Likewise, the number of molecules per nm^2 for the Br^- counterion system is provided in Suppoting Information Table S3.

Desorption behavior in the Br^- system was then examined through dissipation versus frequency plots to better understand the structural dynamics of the interphase (Figures S16 and S17). In this case, during desorption, we observed the inverse of the adsorption process: a sharp increase in dissipation occurs with minimal change in frequency, suggesting the interfacial layer becomes softer and less rigid as DM-L molecules leave the surface. This behavior is consistent with the departure of a previously well-packed monolayer.[37] Overall, our EQCM-D results suggest that DM-L can not only form ordered assembly at the interphase but also promote more anion decomposition.

It is important to clarify the scope and interpretation of the EQCM-D measurements presented in this work. The EQCM-D experiments were conducted on gold-coated quartz sensors and serve as a model system to directly probe the field-responsive adsorption/desorption behavior and interfacial packing dynamics of the dynamic monolayer molecules under an applied electric field. While the assembly may be

https://doi.org/10.1021/jacs.5c19365
J. Am. Chem. Soc. 2026, 148, 6365–6378

slightly different in the coin cell systems (with lithium or copper substrate), EQCM-D provides direct mechanistic evidence that these molecules assemble and disassemble at electrified interfaces in a field-dependent manner. In practical cells, the presence and role of the dynamic monolayer are inferred and supported by various other techniques, including SEI chemistry observed by cryo-XPS, and lithium deposition morphology revealed by operando optical microscopy.

In addition to EQCM-D, we also employed a three-electrode (lithium as reference electrode, copper as counter and working electrodes) staircase potentio electrochemical impedance spectroscopy (SPEIS) technique to probe the field-responsive behavior of the dynamic monolayers (Figure S18). These field-responsive molecules, each bearing a charged or polar group, can participate in the electrical double layer, and their presence may alter the observed double layer capacitance when introduced into the system. This method enables tracking of double layer capacitance across a potential window, making it effective for detecting interfacial changes induced by an electric field.[41] As shown in Figure 2h–j, capacitance increases as the potential approaches the lithium plating potential, consistent with the accumulation of charged species at the interphase.

The magnitude of capacitance change is strongly dependent on molecular size. The molecular volumes of all species were calculated using DFT and provided in Figure S19. For the largest molecule (DM-L), the overall capacitance change is similar to that of the baseline 1.2 M F5DEE electrolyte. While DM-L responds to the applied field, its larger size limits how many molecules can accumulate in the double layer region. In contrast, the smaller molecules (DM-S and DM-SF) exhibit a more pronounced increase in capacitance, suggesting that their compact structures allow greater accumulation at the interphase. As a complementary technique to EQCM-D, SPEIS analysis further supports the field-responsive behavior of these materials. More importantly, it demonstrates how molecular size influences their ability to participate in the electrical double layer.

Demonstrating Enhanced Electrochemical Stability and Performance

It is important to understand how dynamic monolayers affect lithium metal battery performance across a range of cell configurations, including Li||Cu, Li||Li, 20 μm||NMC811, and Cu||NMC811. In all electrochemical tests, 0.1 mM of dynamic monolayer/$Pyr_{1,8}$-FSI is added to 1.2 M LiFSI in F5DEE, while 1.2 M LiFSI in F5DEE alone serves as the control.

We first investigated the impact of dynamic monolayer addition on calendar aging, which refers to the degradation that occurs during extended resting periods without cycling, often leading to capacity loss and reduced CE.[42] While resting the cell at plated state, the monolayer remains at the electrode surface due to the low potential of lithium, which provides a strong driving force for cation adsorption. We hypothesize that the long alkyl tail of the dynamic monolayer can reduce solvent molecule presence near the interphase, reducing solvent-driven corrosion. To test this, Li||Cu cells were cycled at 0.5 mA cm^{-2} with 1 mAh cm^{-2}, with a 24 h rest period after the 10th cycle (Figures 3a and S20). As expected, the CE dropped due to calendar aging; however, this drop was significantly suppressed in cells containing dynamic monolayers (Figures 3b and S21). The reduction in CE for DM-L, DM-S and DM-SF all nearly halved compared to the control and $Pyr_{1,8}$-FSI, highlighting the ability of the monolayers to reduce solvent exposure and mitigate corrosion during rest.

We next examined Li||Cu cycling performance at 2 mA cm^{-2} and 2 mAh cm^{-2} (Figures 3c–e and S22). In the control electrolyte, CE fluctuated significantly due to the high current density and capacity, which are known to promote dead lithium formation from poor lithium deposition morphology.[43,44] With dynamic monolayer addition, particularly DM-L, CE fluctuation was dramatically reduced. Figures 3f and S23 summarize the standard deviation in CE over the first 75 cycles. All monolayer-containing cells showed reduced CE variability. This is especially the case with DM-L, which maintained a stable CE of around 99% even under these harsh conditions (higher rate and capacity). In comparison, DM-S and DM-SF show slight fluctuations, likely due to their weaker packing ability. These results suggest that the improved CE stability, particularly in the DM-L system, is linked to its ability to form a highly ordered interfacial layer. Since CE fluctuation is closely tied to dead lithium formation, we hypothesize that DM-L promotes more uniform lithium deposition, thereby reducing inactive lithium accumulation—a hypothesis further explored in later sections.

To better understand lithium transport behavior, we measured overpotentials in Li||Li symmetric cells across a range of current densities (0.5–2.5 mA cm^{-2}) and dynamic monolayer concentrations (0.1 M, 0.01 M, 1 mM, and 0.1 mM) (Figures 3g–i and S24–S28). For DM-L, we observed a concentration-dependent effect: higher concentrations (0.1 M) increased overpotential, while the lowest concentration (0.1 mM) significantly reduced overpotential (Supporting Information Table S4). This trend was not observed in the DM-S, DM-SF, or $Pyr_{1,8}$-FSI systems, where overpotential remained relatively unchanged across concentrations. These results suggest that at high concentrations, the extended ordering of DM-L at the interphase may begin to hinder lithium-ion transport, whereas at low concentrations, a thin, ordered layer forms that effectively guides lithium flux and reduces transport resistance.

We evaluated the cycling performance of 20 μm Li || NMC811 coin cells with an areal loading of 4.5 mAh cm^{-2} and a 4.4 V cutoff voltage. Under this limited-lithium configuration, the addition of dynamic monolayers nearly doubled the cycle life under C/5 charge–C/3 discharge conditions (Figure 3j). Among the three dynamic monolayers tested, DM-L, which exhibits the strongest packing capability, delivered the best capacity retention. We further assessed the impact of dynamic monolayers in anode-free NMC811||Cu cells with the same high loading and voltage cutoff. This configuration eliminates excess lithium metal, pushing the system even closer to practical energy density targets. Under both C/5 charge–C/3 discharge (Figure 3j) and C/3 charge–C/3 discharge (Figure S30) conditions, cells with dynamic monolayers showed improved capacity retention. Voltage–capacity profiles at cycles 5, 10, 20, and 40 (Figures S31–S33) indicate reduced voltage polarization and better capacity retention, consistent with improved interfacial behavior. Notably, in the C/3–C/3 protocol, an ~1.5% increase in CE was observed in dynamic monolayer-containing cells relative to the already high-performing F5DEE control. This enhancement may arise from both reduced overpotential and improved oxidative stability, the latter supported by linear sweep voltammetry in Li||Pt cells (Figure S29).

https://doi.org/10.1021/jacs.5c19365
J. Am. Chem. Soc. 2026, 148, 6365–6378

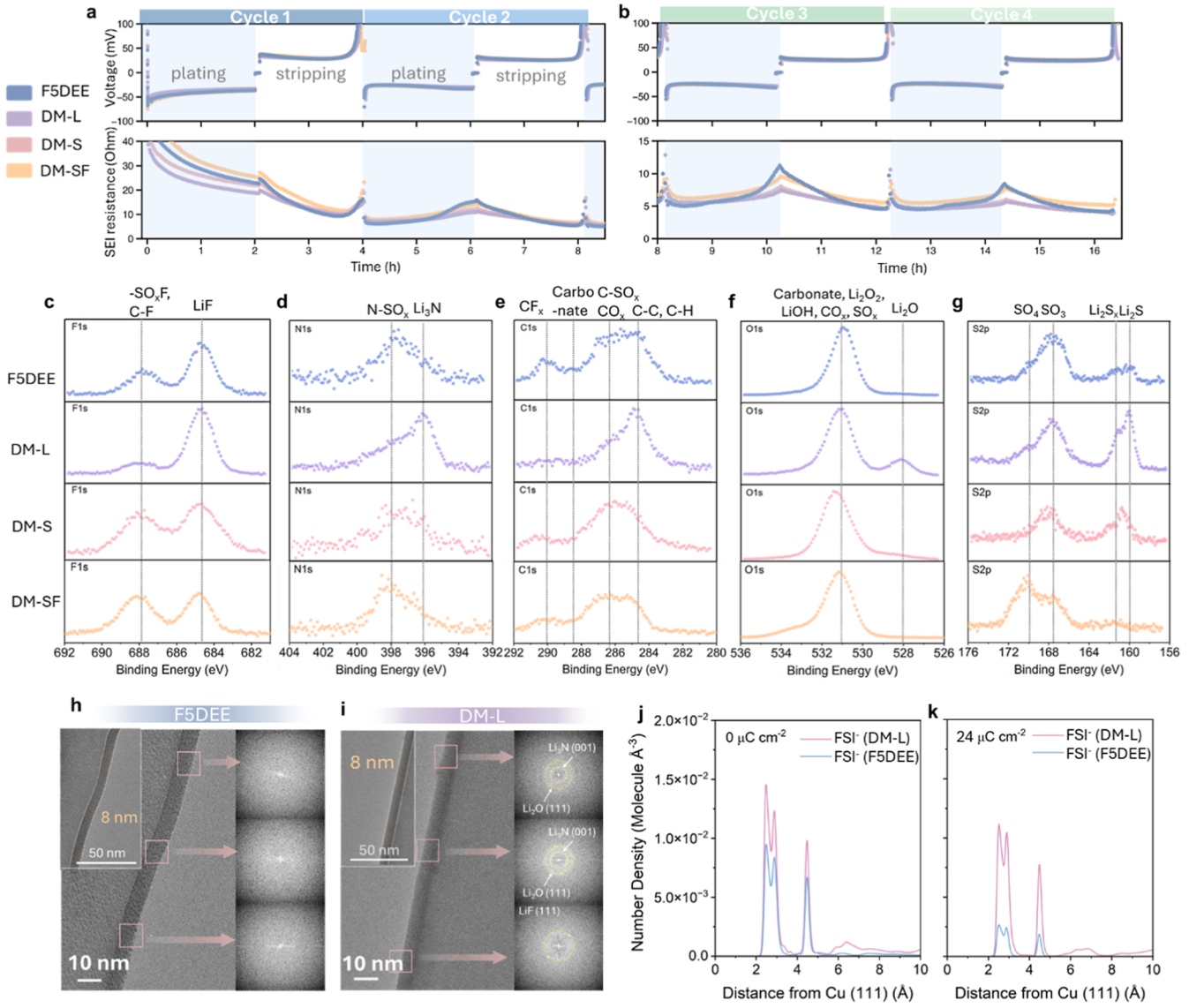

Figure 4. For all SEI characterizations, 0.1 mM of dynamic monolayer was added to 1.2 M LiFSI/F5DEE. (a,b) Dynamic electrochemical impedance spectroscopy showing the evolution of SEI resistance over the course of 4 cycles at 0.5 mA cm^{-2} and 1 mAh cm^{-2}. Reduced SEI resistance is observed for cells with dynamic monolayers, especially with DM-L. (c–g) Cryo-XPS of all four electrolytes. Cells with DM-L show significant increase in inorganic contents, including LiF, Li_3N, Li_2O, and Li_2S. (h,i) Cryo-TEM showing SEI thickness comparison (h) without and (i) with DM-L. Although the direct SEI thickness values are comparable, more inorganic components are identified with DM-L addition. (j,k) Molecular dynamics simulation showing the number density of FSI^- as a function of distance from Cu (111) at (j) 0 μC cm^{-2} and (k) 24 μC cm^{-2}. Increased FSI^- presence near the electrode surface is observed when DM-L is added.

To determine whether these performance changes stem from bulk electrolyte modifications, we also measured the conductivity and viscosity of electrolytes with dynamic monolayers. As shown in Figures S8 and S9, no significant changes were observed, indicating that the performance improvements originate from interphase modification rather than bulk properties. These results underscore the importance of in situ formation of an ordered interfacial layer, and motivate further investigation into how the dynamic monolayer alters interfacial chemistry and lithium morphology.

Understanding Interphase Composition and Evolution

One of the key advantages of dynamic monolayers is their ability to influence SEI formation. To evaluate their impact, we first examined the SEI resistance using dynamic electrochemical impedance spectroscopy (dEIS). Unlike conventional EIS, which provides only a static snapshot, dynamic EIS enables real-time tracking of resistance changes during cell cycling, offering a more detailed view of how the SEI evolves under operating conditions.[45]

As shown in Figure 4a,b, we monitored the SEI resistance over the first four cycles of Li||Cu cells cycled at 0.5 mA cm^{-2} and 1 mAh cm^{-2}. Results are shown for the control electrolyte (1.2 M LiFSI in F5DEE) and for the same electrolyte with 0.1 mM of each dynamic monolayer added. Compared to the control, both DM-L and DM-S exhibited substantially lower SEI resistance, particularly at the end of lithium plating and the beginning of stripping. In contrast, DM-SF, which has weaker packing ability, showed slightly elevated SEI resistance. The reduction in resistance observed in DM-L and DM-S may arise from differences in SEI composition or the formation of a thinner, more compact interphase,[46] both of which are

https://doi.org/10.1021/jacs.5c19365
J. Am. Chem. Soc. 2026, 148, 6365–6378

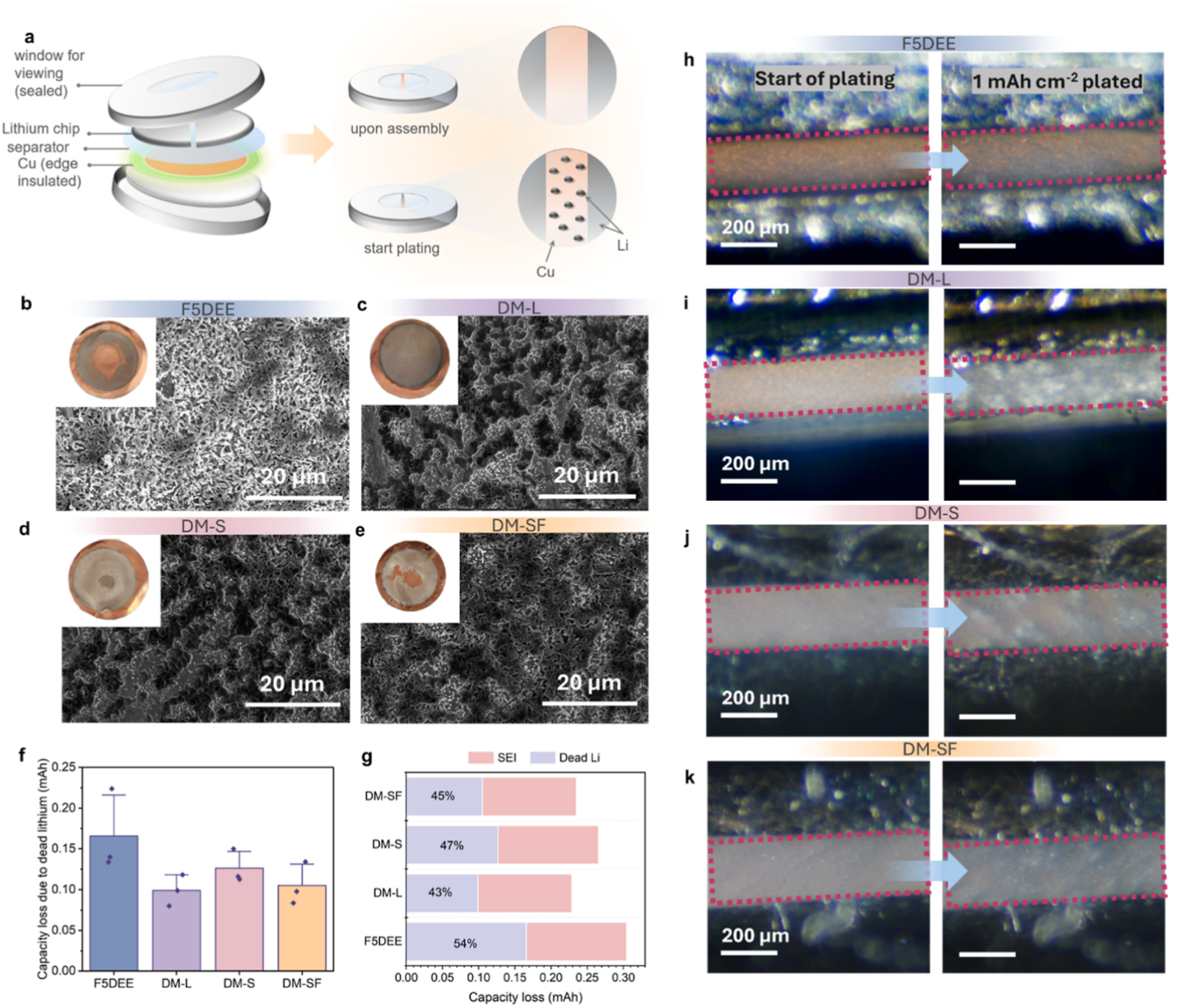

Figure 5. For all lithium morphology characterizations, 0.1 mM of dynamic monolayer was added to 1.2 M LiFSI/F5DEE. (a) Schematic illustrating operando optical cell setup and how lithium nucleation was directly observed. (b−e) Scanning electron microscopy images for all four electrolytes showing larger lithium chunks deposited with dynamic monolayer addition. All images were obtained with 0.1 mAh cm^{-2} lithium plated onto copper at 1 mA cm^{-2}. Images of the plated copper foil are also shown on the left corner for visualization of lithium deposition uniformity. (f,g) Titration gas chromatography to determine dead lithium amount for cells with and without dynamic monolayer. Significant reduction in dead lithium content was observed for all cells with dynamic monolayers. The dead lithium contents were quantified after 20 cycles at 1 mA cm^{-2} and 1 mAh cm^{-2}. All results are shown as the average of three replicate cells. (h−k) Lithium nucleation and deposition over time observed under operando optical microscope. Images of lithium deposition onto copper are shown at the start of plating and after 1 mAh cm^{-2} of lithium is plated.

investigated in this section. Given the consistent trend across the three molecules, we attribute this improvement primarily to the packing ability of the dynamic monolayers.

To further explore the origins of this reduced SEI resistance, we performed cryogenic X-ray photoelectron spectroscopy (cryo-XPS) to investigate the chemical composition of the SEI. Cryo-XPS, recently developed by Shuchi et al., enables more accurate characterization of SEI chemistry by minimizing beam damage and preserving native interphase structure.[47] Samples were maintained near liquid nitrogen temperatures throughout the measurement. We collected F 1s, N 1s, C 1s, O 1s, and S 2p spectra for all systems. As shown in Figure 4c−g, the SEI formed in the presence of DM-L contains significantly more inorganic anion-derived decomposition products (LiF, Li_3N, Li_2O, and Li_2S) than the control electrolyte. Quantitative analysis of elemental ratios confirms this trend: the (N + F + S)/C ratio in the DM-L system is more than twice that of the control (Figures S34 and S35). A slight increase in inorganic compounds was observed in the DM-S system (particularly Li_2S), although not as significant as DM-L. Interestingly, this increased anion decomposition was not observed in DM-SF, whose XPS spectra and elemental ratios were nearly identical to the control. This further supports the hypothesis that the dynamic monolayers with strong packing ability can enrich anion concentration at the interphase, thereby facilitating anion decomposition. This observation is consistent with EQCM-D data, where mass changes attributed to FSI^- decomposition were also more pronounced in the DM-L system.

https://doi.org/10.1021/jacs.5c19365
J. Am. Chem. Soc. 2026, 148, 6365−6378

To complement the chemical analysis, we also examined SEI thickness using cryogenic transmission electron microscopy (cryo-TEM)[48,49] and focused ion beam (FIB). As shown in Figures 4h,i and S36−S39, the average direct SEI thickness in the DM-L system was similar to that of the control (∼8 nm). Cryo-TEM imaging also revealed crystalline domains within the SEI of the DM-L system corresponding to Li_3N (001), Li_2O (111), and LiF (111), in agreement with cryo-XPS results. In addition to cryo-TEM, the SEI thickness after 10 cycles was also analyzed by cutting a cross section with FIB. As shown in Figure S40, the SEI thickness with DM-L added was almost half that of the 1.2 M LiFSI/F5DEE control, suggesting the ability of DM-L to facilitate a more compact SEI formation over cycling.

Together, the cryo-XPS and cryo-TEM analyses confirm that enhancing the packing strength of dynamic monolayers can help recruit anions to the interphase, promoting the formation of a more inorganic, crystalline SEI—an interfacial structure that likely contributes to both improved stability and reduced resistance during cycling. Figure S41 illustrates a proposed mechanism underlying the observed behavior. Dynamic monolayers with strong packing ability, such as DM-L, are hypothesized to form an ordered assembly at the interphase. These molecules are initially paired with FSI^- anions, which they bring to the interphase upon assembly. Beyond these directly associated anions, the packed molecular structure is also expected to create channels that facilitate lithium ion transport. As lithium ions migrate toward the electrode, they carry additional FSI^- anions through coordination, increasing the local concentration of reducible anions near the interphase. This enhanced anion presence may lead to increased FSI^- decomposition.

To confirm the proposed mechanism, we performed molecular dynamics (MD) simulations to examine the local chemical environment near the electrode surface under both unbiased and biased conditions. Specifically, we analyzed the number density profiles of FSI^-, Li^+, and dynamic monolayer molecules (when present) as a function of distance from the Cu (111) surface. As shown in Figure 4j,k, even at 0 μC cm^{-2}, systems with DM-L already exhibit higher FSI^- accumulation near the electrode compared to those without. Upon applying a surface charge of 24 μC cm^{-2}, the enrichment of FSI^- becomes more pronounced in the DM-L system. Additional density profiles for Li^+ and other dynamic monolayers (DM-S and DM-SF) are provided in Figure S42. Overall, both DM-L and DM-S systems exhibit increased FSI^- localization at the interface under bias, while the weaker packing ability of DM-SF appears to limit its capacity to recruit FSI^- effectively.

Regulating Lithium Morphology through Dynamic Monolayers

In addition to continuous SEI formation, mossy lithium growth—leading to significant dead lithium formation—is also a major contributor to capacity loss in lithium metal batteries. To investigate whether dynamic monolayers improve lithium deposition, we first used operando optical microscopy, which can directly visualize the nucleation and growth of lithium in real time. This direct observation is particularly valuable, as it allows us to track spatial distribution, uniformity, and morphological evolution during plating.

The operando optical cell used for this study is shown schematically in Figure 5a. A Li||Cu half-cell was assembled with a cathode cap that includes a viewing window to observe lithium growth in real time. The lithium chip was cut in half to create a central slit, allowing visualization of lithium deposition onto the copper current collector. To minimize edge effects—where lithium deposition morphology typically worsens[50]—the edges of the copper foil were taped. Once assembled, lithium deposition could be monitored through the slit as plating proceeds.

Figure 5h−k show the evolution of lithium deposition across four electrolyte systems: the control (1.2 M LiFSI in F5DEE) and the same electrolyte with 0.1 mM of each dynamic monolayer added. Full plating process videos are provided in Supporting Information Videos S1−S4. Early in plating, small lithium nuclei appeared on the copper surface. Among all systems, DM-L exhibited the densest and most uniform nucleation. After plating 1 mAh cm^{-2} of lithium, the differences among the systems became more pronounced. In the control electrolyte, lithium deposition was sparse and scattered, with small, dispersed clusters. In contrast, DM-L resulted in thick, continuous lithium coverage across the entire visible area. DM-S and DM-SF showed intermediate behavior, with partial coverage and moderately sized deposits.

To verify these observations, scanning electron microscopy (SEM) was performed on all samples (Figures 5b−e and S43 and S44). Each SEM image includes a wide-area view (left corner of each image) to assess deposition coverage after plating 0.1 mAh cm^{-2} of lithium at 1 mA cm^{-2}. In both the F5DEE and $Pyr_{1,8}$-FSI systems, lithium deposition was highly localized near the edges, with minimal plating in the central region. In contrast, DM-L showed uniform coverage across the entire copper surface. DM-S showed partial improvement, while DM-SF more resembled the control. At higher magnification, lithium in the dynamic monolayer systems appeared chunkier and denser, in contrast to the mossy and whisker-like morphology seen in the control electrolyte. These results corroborate the optical observations and suggest that dynamic monolayers promote more uniform and compact lithium growth.

A closer look at the center of the current collector—typically a low-pressure region in the coin cell—reveals a trend: the stronger the monolayer's packing ability, the more uniform the lithium deposition. Prior studies have shown that applied pressure can improve lithium morphology;[51] our findings suggest that ordered interfacial assembly can achieve a similar effect, even in regions of lower pressure. A schematic illustrating this concept is shown in Figure S47. With a well-packed dynamic monolayer, lithium flux is more uniformly directed across the surface, reducing localized "hot spots" and promoting even deposition.

It should be noted that the coin-cell configuration used here can introduce spatial variations in mechanical compaction, with lower effective pressure in central regions due to slight bending of the negative can after crimping. As a result, edge-localized lithium deposition represents the baseline plating behavior under these conditions and is consistently observed across multiple cells, rather than a selected example. The introduction of dynamic monolayer molecules modifies lithium deposition behavior within this mechanically heterogeneous environment, but does not eliminate the underlying pressure gradients.

Additional evidence for this guided flux behavior comes from cryo-TEM atlas images of lithium deposited on TEM grids, which maps out all areas on the grid (Figures S45 and S46). Compared to $Pyr_{1,8}$-FSI, which lacks packing ability and

https://doi.org/10.1021/jacs.5c19365
J. Am. Chem. Soc. 2026, 148, 6365−6378

produces widespread lithium whiskers, DM-L shows much chunkier and more uniformly distributed lithium, with significantly fewer whiskers. These observations further support the conclusion that the formation of an ordered interfacial layer is essential for achieving controlled lithium flux and uniform morphology.

To evaluate how these morphological changes impact dead lithium formation, we used titration gas chromatography (TGC) to quantify the amount of inactive lithium.[7] In this method, residual SEI (on copper foils) was extracted from half-cells cycled at 1 mA cm^{-2} and 1 mAh cm^{-2} for 20 cycles. All active lithium was stripped prior to disassembly, ensuring that any remaining lithium was electrically isolated and counted as "dead." Each sample was placed in a sealed GC vial, where 1 mL of water was injected. Upon reaction, evolved hydrogen gas was analyzed via GC to quantify the amount of metallic lithium present. This enables back-calculation of dead lithium content within the SEI matrix.

As shown in Figure 5f,g, the amount of dead lithium was significantly reduced in all dynamic monolayer systems, with DM-L showing over a 10% decrease in dead lithium contribution to capacity loss. This trend aligns with the optical and SEM results, where DM-L consistently produced more uniform, chunkier lithium deposits. A more compact lithium morphology minimizes the formation of electrically isolated regions during stripping, thereby reducing dead lithium and improving long-term cycling efficiency.

Taken together, these results show that dynamic monolayers can regulate lithium deposition and suppress dead lithium formation. Operando optical microscopy directly captures the nucleation and growth process, with DM-L showing the most uniform and continuous lithium deposition due to its highly ordered interfacial assembly.

We would also like to note that at the cell level, the adsorption of dynamic monolayer molecules and SEI growth are likely coupled and occur concurrently during early interphase evolution. Under these conditions, the dynamic monolayer molecules may also function as electrolyte additives in a conventional sense. However, their proposed distinguishing characteristic is an intrinsic, field-responsive tendency to assemble at electrified interfaces, as demonstrated on a model system by EQCM-D. At the cell level, this behavior is reflected indirectly through consistent changes in SEI composition, lithium deposition morphology, and electrochemical response.

Overall, dynamic monolayers are shown to improve multiple aspects of lithium metal battery performance. A key trend observed across our study is the strong correlation between molecular packing ability and electrochemical outcomes: molecules that form more ordered assemblies at the interphase consistently lead to better performance. The impact of packing strength on cell efficiency, SEI composition, and lithium deposition morphology is summarized in Supporting Information Table S5. These results underscore the critical role of ordered interfacial assembly in stabilizing lithium metal batteries.

CONCLUSION

In this work, we developed a new class of field-responsive dynamic monolayers consisting of a stable headgroup, controlled chain length, and aromatic units for packing properties. These molecules can reversibly adsorb and desorb in response to an applied electric field. Unlike other reported additives that are either lacking ordered tails or ordered but permanently anchored, these dynamic monolayers combine structural order with voltage control, enabling a more adaptive and responsive interphase for lithium metal batteries.

Through EQCM-D studies, we directly captured the adsorption and desorption behavior of the dynamic monolayers with nanogram-level precision. These measurements revealed not only the field-responsive nature of the materials, but also showed that molecules with stronger packing ability, such as DM-L, could form more rigid and densely packed layers under bias.

SEI characterization by dynamic EIS, cryo-XPS and cryo-TEM provided chemical and structural insights into the effects of dynamic monolayers. In particular, DM-L was found to enrich the interphase with anion-derived inorganic species such as LiF, Li_3N, and Li_2O. This change in SEI composition and structure correlated with reduced interfacial resistance during cycling.

Lithium morphology studies using operando optical microscopy and SEM revealed that dynamic monolayers, especially DM-L, guided lithium deposition into denser and more uniform structures. Real-time operando optical imaging captured the progression of plating, while SEM and cryo-TEM confirmed that monolayer-treated systems exhibited chunkier, less mossy lithium growth. Titration gas chromatography further quantified the impact of improved morphology, showing a significant reduction in dead lithium formation.

These improvements lead to more stable cycling behavior and reduced overpotentials in both half-cell and full-cell configurations. Together, our findings establish dynamic monolayers as a versatile and effective strategy for addressing interfacial challenges in lithium metal batteries, offering a new direction for responsive interphase design.

EXPERIMENTAL PROCEDURES

Materials

4-[(8-Bromooctyl)oxy]-4′-methyl-1,1′-biphenyl was purchased from AOBChem USA. $Pyr_{1,8}$-FSI was obtained from Aurora Fine Chemicals LLC. 1-(4-Bromobutyl)-4-methylbenzene and 1-(4-bromobutyl)-4-(trifluoromethyl)benzene were purchased from Aaron Chemicals. 1-Methylpyrrolidine was sourced from Thermo Fisher Scientific. Amberlite HPR4811 Ion Exchange Resin was purchased from Sigma-Aldrich. All chemicals used for reactions were used as received without further purification. LiFSI was obtained from Solvionic, and F5DEE was provided by Feon Energy.

Battery components for coin cell assembly included 2032-type cases, cone springs, spacers, and Al-clad cases, all purchased from MTI Corporation. Celgard 2325 separators (25 μm thick, with polypropylene/polyethylene/polypropylene layers) were used as separators and were sourced from Celgard. Thick lithium foils (750 μm) and copper current collectors (25 μm) were obtained from Alfa Aesar. Thin Li foils (20 μm thick) were sourced from China Energy Lithium. Commercial NMC811 cathodes with an areal capacity of approximately 4 mAh cm^{-2} were supplied by Targray.

Dynamic Monolayer Synthesiss

Synthesis of Dynamic Monolayer Molecules (DM-L, DM-S, DM-SF with Br^- Counterion): DM-L, DM-S, and DM-SF were synthesized by reacting 1-methylpyrrolidine with 4-[(8-bromooctyl)oxy]-4′-methyl-1,1′-biphenyl, 1-(4-bromobutyl)-4-methylbenzene, and 1-(4-bromobutyl)-4-(trifluoromethyl)benzene, respectively. For each reaction, starting bromide compound (1a, 1b, or 1c, 0.5 mmol) was dissolved in 5 mL of anhydrous toluene and added slowly to a stirred solution containing anhydrous toluene (25 mL) and 1-methylpyrrolidine (5 mmol) under a nitrogen atmosphere. For the synthesis of DM-SF, an additional anhydrous methanol (10 mL) was added to improve solubility. The reaction mixture was maintained under

https://doi.org/10.1021/jacs.5c19365
J. Am. Chem. Soc. 2026, 148, 6365−6378

nitrogen and stirred at 80 °C for 48 h. After completion, the reaction was cooled to room temperature over 1 h. The precipitated product was collected by filtration through a nylon filter membrane and washed thoroughly with ethyl acetate and toluene. The resulting solid was dried under vacuum at room temperature for 24 h. Typical yields were approximately 50%.

Ion Exchange to FSI^- Counterion: Amberlite HPR4811 Ion Exchange Resin was first converted into its iodide form. Amberlite HPR4800 Cl resin (5 g) was placed in an Erlenmeyer flask and washed thoroughly with deionized water. An aqueous KI solution (10 wt %, 50 mL) was then added to the resin, and the mixture was stirred for 1 h. The solution was decanted, and the iodide exchange process was repeated two additional times (three times total). To remove excess KI, the resin was subsequently washed with deionized water (3 times) and methanol (2 times) using the same procedure. The resulting iodide-form resin was dried under dynamic vacuum at 70 °C overnight.

To exchange the bromide counterion to bis(fluorosulfonyl)imide (FSI^-), approximately 2 g of the iodide-form resin was stirred with 2 g of LiFSI dissolved in 15 mL of anhydrous acetone under nitrogen at room temperature for 1 h. This ion-exchange process was repeated three times, each time replacing the LiFSI/acetone solution with fresh material, to ensure complete loading of FSI^- onto the resin. The ion exchange is confirmed with XPS, where peaks corresponding to Br^- disappear after the exchange of Br^- to FSI^-.

Subsequently, 1 g of the FSI^--grafted resin was stirred with 100 mg of DM-L, DM-S, or DM-SF dissolved in 15 mL of dichloromethane (DCM) at room temperature under nitrogen for 1 h. The same DCM solution was reused with freshly exchanged FSI^--resin two additional times to maximize counterion exchange. After the final treatment, DCM was evaporated under reduced pressure to isolate DM-L, DM-S, and DM-SF with FSI^- as the counterion. The purity of all synthesized compounds were confirmed by ^1H NMR (nuclear magnetic resonance) using a Varian 400 MHz NMR spectrometer and ATR-FTIR.

Electrochemical Quartz Crystal Microbalance with Dissipation Monitoring

All EQCM-D experiments are carried out with Qsense Explorer from Biolin Scientific. The window cell module was assembled using a platinum window as the counter electrode and a gold-coated quartz crystal sensor as the working electrode. The assembled cell was left to rest for 30 min to allow baseline stabilization. Solution of interest was then introduced into the cell using a peristaltic pump, followed by an additional rest period until a stable baseline was reached (defined as a frequency drift of less than 3 Hz per hour). The EQCM-D was interfaced with a Landt battery testing system for voltage control during electrochemical measurements.

Electrochemical Measurements and Characterization

All battery components used in this work were commercially available and all electrochemical tests were carried out using 2032-type coin cells. The cells were fabricated in an argon-filled glovebox, and one layer of Celgard 2325 was used as a separator for all batteries. Thick Li foil (750 μm) with a diameter of 7/16 in. was used for Li||Cu and Li||Li cell assembly, and 40 μL of electrolyte was injected in all cells. All cells were tested on Landt battery testing station under room temperature.

To begin long-term cycling experiments, the copper surface was first preconditioned by cycling between 0 and 1 V at a current density of 0.2 mA cm^{-2} for 10 cycles. Following this conditioning step, 2 mAh cm^{-2} of lithium was deposited onto the copper at 2 mA cm^{-2} and then stripped back to 1 V at the same rate. Ionic conductivity was determined from the bulk resistance measured in symmetric cells assembled with two stainless steel electrodes and a separator soaked in electrolyte, using a Biologic potentiostat. Viscosity measurements were performed using a Rheometer-on-a-chip (model m-VROC-II), where samples (~40 μL) were introduced through a syringe pump at controlled flow rates. Step potential electrochemical impedance spectroscopy (SPEIS) experiments were conducted using three-electrode cells, with copper foil as both the working and counter electrodes, and a small piece of lithium metal serving as the reference electrode. PEIS measurements were collected at various applied potentials over a frequency range of 1 MHz to 100 mHz, also using the Biologic system.

All full cells were cycled using the follow protocol: Li||NMC or Cu|| NMC coin cells were first cycled at 0.1C charge/discharge rates for activation. Cells were cycled within voltage ranges of 2.8−4.4 V, with an electrolyte to cathode ratio (E/C) of approximately 8 g Ah^{-1}.

For dynamic EIS, Li||Cu cells were assembled and discharged from their OCV (2−3 V) with an applied DC current of 0.5 mA cm^{-2} until a total capacity of 1 mAh was reached. Then, the cells were charged at 0.5 mA cm^{-2} until the cell voltage exceeded 1 V. GEIS measurements were taken every minute during using a 0.4 mA current amplitude from 200 kHz to 1 Hz. The resulting impedance was fit using an equivalent circuit with one resistor and two RC components.

All SEM images were obtained using the Thermo Fisher Scientific Apreo system.

Cryogenic X-ray Photoelectron Spectroscopy

Cryo-XPS was performed using a PHI VersaProbe 4 instrument. To prepare samples, Li||Cu half-cells were first assembled and cycled to deposit 0.5 mAh cm^{-2} of lithium at a current density of 1 mA cm^{-2}. After cycling, the cells were disassembled, and the copper surface (with lithium plated on top) was rinsed twice with 30 μL of pure F5DEE solvent. Residual solvent was carefully blotted away using a balloon to remove excess solvent. The electrodes were then halved, placed into sealed Falcon tubes, and rapidly immersed into liquid nitrogen. After freezing, the tubes were broken open under liquid nitrogen, and the samples were transferred into vials filled with liquid nitrogen for storage. For measurement, the samples were quickly mounted onto a cryogenic platen already cooled to liquid nitrogen temperatures. The platen was then transferred into the main XPS chamber, where the sample was maintained at − 110 °C throughout the entire data acquisition process.

Cryogenic Transmission Electron Microscopy

For cryo-TEM experiments, a 400-mesh copper TEM grid was placed directly on top of the copper current collector during coin cell assembly. To prepare samples, Li||Cu half-cells were first assembled and cycled to deposit 0.5 mAh cm^{-2} of lithium at a current density of 1 mA cm^{-2}, after which the cell was disassembled inside an argon-filled glovebox. The retrieved TEM grid was thoroughly rinsed with F5DEE to remove residual salts. To preserve the sample, the dried grid was placed inside a sealed plastic Falcon tube and immediately immersed in a container of liquid nitrogen. The tube was broken open under liquid nitrogen using pliers, and the grid was transferred into a liquid nitrogen dewar for storage. Still submerged in liquid nitrogen, the grid was autoloaded into the TEM column, where the sample temperature was maintained at −172 °C throughout the imaging session.

Cryo-TEM images were acquired either with a Glacios 200 kV Cryo Transmission Electron Microscope equipped with a Falcon 4i Camera Direct Electron Detector through the Velox software, or with a Krios G2 300 kV Cryo Transmission Electron Microscope equipped with a K3 Camera through the Digital Micrograph software. Both microscopes were equipped with an autoloader system for cryoEM grid loading. Atlas maps of the grids were acquired through the Thermo Fisher Tomography or EPU software, to identify dendrite locations on the grids.

Operando Optical Cell Construction

A Li||Cu half-cell was constructed to enable real-time visualization of lithium deposition. The cathode cap was modified by gluing a thin piece of microscope slide glass (0.1 mm thick) over a central opening using epoxy, creating a transparent viewing window. Before assembly, the lithium foil was cut in half to form a central slit, exposing the underlying copper current collector for direct observation of lithium plating. To minimize edge effects—where lithium tends to deposit more unevenly—the edges of the copper foil were taped. Following assembly, lithium nucleation and growth were continuously

https://doi.org/10.1021/jacs.5c19365
J. Am. Chem. Soc. 2026, 148, 6365−6378

monitored through the slit during plating at 0.5 mA cm^{-2} to a total capacity of 1 mAh cm^{-2}.

Titration Gas Chromatography

The amount of inactive lithium was determined using H_2 titration on rSEI samples. Li||Cu half-cells were cycled for 20 cycles at a current density of 0.5 mA cm^{-2} with an areal capacity of 1 mAh cm^{-2}, after which all lithium was fully stripped from the copper. The residual SEI-coated copper foil was placed into a sealed 10 mL vial, and 1 mL of deionized water was added to initiate the reaction. After allowing the reaction to proceed for 3 min, the amount of hydrogen gas evolved was measured using a gas chromatograph (SRI 8610C).

Molecular Dynamics

Classical, fixed-charge MD was conducted using LAMMPS.[53] Each system was initially constructed in random, amorphous configurations with dimensions and compositions listed in Supporting Information Table S6. Interfacial simulations used a fixed boundary condition in the z direction. Solvents, Li^+, and Gx molecules were described using the General Amber force field with partial charges defined by the AM1-BCC method in ANTECHAMBER.[54] FSI^- was described by Gouveia et al.[55] 4-layer FCC Cu (111) slabs were described using the interfacial force field from Heinz et al.[56] Nonbonded interactions were generated using Lorentz−Berthelot mixing rules. In all cases the charges of the ionic species were scaled to 0.75. Charged electrodes were compensated for by adding additional Li^+ atoms to the cell with charge distribution described by Reed et al. via the "fix electrode" command in LAMMPS.[57] Individual MD runs were conducted for each charge condition to ensure proper equilibration. In all cases, long-range Coulomb interactions were computed with a particle−particle-particle-mesh solver, with an error tolerance of 10^{-4}.[58]

Before any dynamics were simulated, a conjugate gradient energy minimization at 0 K was performed with energy and force tolerances of 10^{-4}. In all cases, the Cu electrode atoms were fixed in place for the entire simulation, and a uniform force equivalent to 1 atm was placed on the electrolyte. Afterward, the electrolytes were heated to 298 K over 0.1 ns using a Langevin thermostat, with a damping parameter of 100 fs. Afterward, 3 cycles of annealing-quench dynamics were then applied in both systems between 298 and 894 K with 0.25 ns ramping periods and 0.1 ns at either extreme via a Langevin thermostat with a damping parameter of 10 ps. Finally, bulk systems were subjected to 10 ns of production dynamics at 298 K was performed, again using a Langevin thermostat with a damping parameter of 100 ps. Density profiles were calculated during production dynamics with a bin width of 0.02 Å.

■ ASSOCIATED CONTENT

Supporting Information

The Supporting Information is available free of charge at https://pubs.acs.org/doi/10.1021/jacs.5c19365.

Supporting Information Videos of the lithium deposition evolution under optical microscopy are also included (MP4)

Supporting Information Video S2 (MP4)

Supporting Information Video S3 (MP4)

Supporting Information Video S4 (MP4)

Supporting Information includes additional experimental details, materials, and methods (PDF)

■ AUTHOR INFORMATION

Corresponding Authors

Yi Cui − *Department of Materials Science and Engineering and Department of Energy Science and Engineering, Stanford University, Stanford, California 94305, United States;* orcid.org/0000-0002-6103-6352; Email: yicui@stanford.edu

Zhenan Bao − *Department of Chemical Engineering, Stanford University, Stanford, California 94305, United States;* orcid.org/0000-0002-0972-1715; Email: zbao@stanford.edu

Authors

Elizabeth Zhang − *Department of Chemical Engineering, Stanford University, Stanford, California 94305, United States; Department of Materials Science and Engineering, Stanford University, Stanford, California 94305, United States;* orcid.org/0000-0002-1117-8635

John Holoubek − *Department of Chemical Engineering, Stanford University, Stanford, California 94305, United States; Department of Materials Science and Engineering, Stanford University, Stanford, California 94305, United States;* orcid.org/0000-0003-0015-4512

Hao Lyu − *Department of Chemical Engineering, Stanford University, Stanford, California 94305, United States;* orcid.org/0000-0001-7393-2456

Yuqi Li − *Department of Materials Science and Engineering, Stanford University, Stanford, California 94305, United States;* orcid.org/0000-0003-1501-1549

Jacob Florian − *Department of Chemical Engineering, Stanford University, Stanford, California 94305, United States;* orcid.org/0000-0003-1895-8463

Sanzeeda Baig Shuchi − *Department of Chemical Engineering, Stanford University, Stanford, California 94305, United States; Department of Materials Science and Engineering, Stanford University, Stanford, California 94305, United States*

Jane K.J. Lee − *Department of Structural Biology, Stanford University, Stanford, California 94305, United States*

Lukas Michalek − *Department of Chemical Engineering, Stanford University, Stanford, California 94305, United States;* orcid.org/0000-0002-2257-5038

Tianyang Chen − *Department of Chemical Engineering, Stanford University, Stanford, California 94305, United States;* orcid.org/0000-0003-3142-8176

Zhouyi Chen − *Department of Materials Science and Engineering, Stanford University, Stanford, California 94305, United States*

Il Rok Choi − *Department of Chemical Engineering, Stanford University, Stanford, California 94305, United States; Department of Materials Science and Engineering, Stanford University, Stanford, California 94305, United States*

Xuelin Guo − *Department of Chemical Engineering, Stanford University, Stanford, California 94305, United States*

Luca Mondonico − *Department of Chemical Engineering, Stanford University, Stanford, California 94305, United States; Department of Materials Science and Engineering, Stanford University, Stanford, California 94305, United States*

Complete contact information is available at: https://pubs.acs.org/10.1021/jacs.5c19365

Notes

The authors declare no competing financial interest.

■ ACKNOWLEDGMENTS

The work was supported by the Assistant Secretary for Energy Efficiency and Renewable Energy, Office of Vehicle Technologies of the U.S. Department of Energy under the Battery

500 Consortium program. Y.C. acknowledges cryo-EM support from the US Department of Energy, Office of Basic Energy Sciences, Division of Materials Science and Engineering under contract DE-AC02-76SF00515. E.Z. acknowledges the support from National Science Foundation Graduate Research Fellowships Program (NSF GRFP). Part of this work was performed at the Stanford Nano Shared Facilities (SNSF), supported by the National Science Foundation under Award ECCS-2026822. We thank Feon Energy for providing F5DEE. We acknowledge the use of the Stanford Cryo-Electron Microscopy Center (cEMc) and the support of cEMc staff for cryo-TEM experiments.

REFERENCES

(1) Liu, J.; et al. Pathways for practical high-energy long-cycling lithium metal batteries. *Nat. Energy* **2019**, *4*, 180−186.
(2) Wang, H.; et al. Liquid electrolyte: The nexus of practical lithium metal batteries. *Joule* **2022**, *6*, 588−616.
(3) Lin, D.; Liu, Y.; Cui, Y. Reviving the lithium metal anode for high-energy batteries. *Nat. Nanotechnol.* **2017**, *12*, 194−206.
(4) Niu, C.; et al. Balancing interfacial reactions to achieve long cycle life in high-energy lithium metal batteries. *Nat. Energy* **2021**, *6*, 723−732.
(5) Wu, H.; Jia, H.; Wang, C.; Zhang, J.; Xu, W. Recent Progress in Understanding Solid Electrolyte Interphase on Lithium Metal Anodes. *Adv. Energy Mater.* **2021**, *11*, 2003092.
(6) Bai, P.; Li, J.; Brushett, F. R.; Bazant, M. Z. Transition of lithium growth mechanisms in liquid electrolytes. *Energy Environ. Sci.* **2016**, *9*, 3221−3229.
(7) Fang, C.; et al. Quantifying inactive lithium in lithium metal batteries. *Nature* **2019**, *572*, 511−515.
(8) Fang, C.; Wang, X.; Meng, Y. S. Key Issues Hindering a Practical Lithium-Metal Anode. *Trends Chem.* **2019**, *1*, 152−158.
(9) Xiao, J.; et al. Understanding and applying coulombic efficiency in lithium metal batteries. *Nat. Energy* **2020**, *5*, 561−568.
(10) Yu, Z.; et al. Rational solvent molecule tuning for high-performance lithium metal battery electrolytes. *Nat. Energy* **2022**, *7*, 94−106.
(11) Ren, X.; et al. Enabling High-Voltage Lithium-Metal Batteries under Practical Conditions. *Joule* **2019**, *3*, 1662−1676.
(12) Choi, I. R.; et al. Asymmetric ether solvents for high-rate lithium metal batteries. *Nat. Energy* **2025**, *10*, 365−379.
(13) Zhang, E.; Chen, Y.; Holoubek, J.; Yu, Z.; Zhang, W.; Lyu, H.; Choi, I. R.; Kim, S. C.; Serrao, C.; Cui, Y.; et al. Monofluorinated acetal electrolyte for high-performance lithium metal batteries. *Proc. Natl. Acad. Sci. U.S.A.* **2025**, *122*, No. e2418623122.
(14) Holoubek, J.; et al. Tailoring electrolyte solvation for Li metal batteries cycled at ultra-low temperature. *Nat. Energy* **2021**, *6*, 303−313.
(15) Zhao, Y.; Zhou, T.; Ashirov, T.; Kazzi, M. E.; Cancellieri, C.; Jeurgens, L. P. H.; Choi, J. W.; Coskun, A. Fluorinated ether electrolyte with controlled solvation structure for high voltage lithium metal batteries. *Nat. Commun.* **2022**, *13*, 2575.
(16) Lopez, J.; et al. Effects of Polymer Coatings on Electrodeposited Lithium Metal. *J. Am. Chem. Soc.* **2018**, *140*, 11735−11744.
(17) Huang, Z.; et al. A salt-philic, solvent-phobic interfacial coating design for lithium metal electrodes. *Nat. Energy* **2023**, *8*, 577−585.
(18) Li, J.; Cai, Y.; Wu, H.; Yu, Z.; Yan, X.; Zhang, Q.; Gao, T. Z.; Liu, K.; Jia, X.; Bao, Z. Polymers in Lithium-Ion and Lithium Metal Batteries. *Adv. Energy Mater.* **2021**, *11*, 2003239.
(19) Kim, M. S.; et al. Suspension electrolyte with modified Li+ solvation environment for lithium metal batteries. *Nat. Mater.* **2022**, *21*, 445−454.
(20) Liu, Y.; Lin, D.; Li, Y.; Chen, G.; Pei, A.; Nix, O.; Li, Y.; Cui, Y. Solubility-mediated sustained release enabling nitrate additive in carbonate electrolytes for stable lithium metal anode. *Nat. Commun.* **2018**, *9*, 3656.
(21) Zhang, H.; et al. Electrolyte Additives for Lithium Metal Anodes and Rechargeable Lithium Metal Batteries: Progress and Perspectives. *Angew. Chem., Int. Ed.* **2018**, *57*, 15002−15027.
(22) Zheng, J.; Engelhard, M. H.; Mei, D.; Jiao, S.; Polzin, B. J.; Zhang, J. G.; Xu, W. Electrolyte additive enabled fast charging and stable cycling lithium metal batteries. *Nat. Energy* **2017**, *2*, 17012.
(23) Ding, F.; et al. Effects of Cesium Cations in Lithium Deposition via Self-Healing Electrostatic Shield Mechanism. *J. Phys. Chem. C* **2014**, *118*, 4043−4049.
(24) Ding, F.; et al. Dendrite-Free Lithium Deposition via Self-Healing Electrostatic Shield Mechanism. *J. Am. Chem. Soc.* **2013**, *135*, 4450−4456.
(25) Dai, H.; Xi, K.; Liu, X.; Lai, C.; Zhang, S. Cationic Surfactant-Based Electrolyte Additives for Uniform Lithium Deposition via Lithiophobic Repulsion Mechanisms. *J. Am. Chem. Soc.* **2018**, *140*, 17515−17521.
(26) Jang, J.; Shin, J.-S.; Ko, S.; Park, H.; Song, W.-J.; Park, C. B.; Kang, J. Self-Assembled Protective Layer by Symmetric Ionic Liquid for Long-Cycling Lithium−Metal Batteries. *Adv. Energy Mater.* **2022**, *12*, 2103955.
(27) Jang, J.; et al. Miniature Li+ solvation by symmetric molecular design for practical and safe Li-metal batteries. *Nat. Energy* **2025**, *10*, 502−512.
(28) Yi, R.; Mao, Y.; Shen, Y.; Chen, L. Self-Assembled Monolayers for Batteries. *J. Am. Chem. Soc.* **2021**, *143*, 12897−12912.
(29) Liu, Y.; et al. Self-assembled monolayers direct a LiF-rich interphase toward long-life lithium metal batteries. *Science* **2022**, *375*, 739−745.
(30) Li, Y.; et al. In situ formation of liquid crystal interphase in electrolytes with soft templating effects for aqueous dual-electrode-free batteries. *Nat. Energy* **2024**, *9*, 1350−1359.
(31) Wang, X.; et al. Poly(Ionic Liquid)s-in-Salt Electrolytes with Co-coordination-Assisted Lithium-Ion Transport for Safe Batteries. *Joule* **2019**, *3*, 2687−2702.
(32) Hoppe, C. E.; Williams, R. J. J. Tailoring the self-assembly of linear alkyl chains for the design of advanced materials with technological applications. *J. Colloid Interface Sci.* **2018**, *513*, 911−922.
(33) Claessens, C. G.; Stoddart, J. F. Interactions In Self-Assembly. *J. Phys. Org. Chem.* **1997**, *10*, 254−272.
(34) Ritchie, T. J.; Macdonald, S. J. F.; Young, R. J.; Pickett, S. D. The impact of aromatic ring count on compound developability: further insights by examining carbo- and hetero-aromatic and -aliphatic ring types. *Drug Discovery Today* **2011**, *16*, 164−171.
(35) Zhao, Y.; Zhou, T.; Mensi, M.; Choi, J. W.; Coskun, A. Electrolyte engineering via ether solvent fluorination for developing stable non-aqueous lithium metal batteries. *Nat. Commun.* **2023**, *14*, 299.
(36) Vergara, M. H.; Sánchez Pacheco, A. D.; Hernández-Ortega, S.; Valdes-Martínez, J. Influence of Fluorine Substitution on Π-Π Stacking and Molecular Packing in Schiff Base Cocrystals. *SSRN Electron. J.* **2025**.
(37) Michalek, L.; Barner, L.; Barner-Kowollik, C. Polymer on Top: Current Limits and Future Perspectives of Quantitatively Evaluating Surface Grafting. *Adv. Mater.* **2018**, *30*, 1706321.
(38) Kitz, P. G.; Lacey, M. J.; Novák, P.; Berg, E. J. Operando EQCM-D with Simultaneous in Situ EIS: New Insights into Interphase Formation in Li Ion Batteries. *Anal. Chem.* **2019**, *91*, 2296−2303.
(39) Shpigel, N.; Levi, M. D.; Sigalov, S.; Daikhin, L.; Aurbach, D. In Situ Real-Time Mechanical and Morphological Characterization of Electrodes for Electrochemical Energy Storage and Conversion by Electrochemical Quartz Crystal Microbalance with Dissipation Monitoring. *Acc. Chem. Res.* **2018**, *51*, 69−79.
(40) Tao, N. J.; Lindsay, S. M. In situ scanning tunneling microscopy study of iodine and bromine adsorption on gold(111) under potential control. *J. Phys. Chem.* **1992**, *96*, 5213−5217.
(41) Attias, R.; Dlugatch, B.; Chae, M. S.; Goffer, Y.; Aurbach, D. Changes in the interfacial charge-transfer resistance of Mg metal

electrodes, measured by dynamic electrochemical impedance spectroscopy. *Electrochem. Commun.* **2021**, *124*, 106952.
(42) Boyle, D. T.; et al. Corrosion of lithium metal anodes during calendar ageing and its microscopic origins. *Nat. Energy* **2021**, *6*, 487−494.
(43) Chen, Y.; et al. Failure Process During Fast Charging of Lithium Metal Batteries with Weakly Solvating Fluoroether Electrolytes. *J. Phys. Chem. C* **2024**, *128*, 11487−11497.
(44) Zhang, W.; et al. Recovery of isolated lithium through discharged state calendar ageing. *Nature* **2024**, *626*, 306−312.
(45) Talian, S. D.; Kapun, G.; Moškon, J.; Dominko, R.; Gaberščček, M. Operando impedance spectroscopy with combined dynamic measurements and overvoltage analysis in lithium metal batteries. *Nat. Commun.* **2025**, *16*, 2030.
(46) Bieker, G.; Winter, M.; Bieker, P. Electrochemical in situ investigations of SEI and dendrite formation on the lithium metal anode. *Phys. Chem. Chem. Phys.* **2015**, *17*, 8670−8679.
(47) Shuchi, S. B.; D'Acunto, G.; Sayavong, P.; et al. Cryogenic X-ray photoelectron spectroscopy for battery interfaces. *Nature* **2025**, *646*, 850−855.
(48) Li, Y.; et al. Atomic structure of sensitive battery materials and interfaces revealed by cryo−electron microscopy. *Science* **2017**, *358*, 506−510.
(49) Zhang, E.; et al. Expanding the cryogenic electron microscopy toolbox to reveal diverse classes of battery solid electrolyte interphase. *iScience* **2022**, *25*, 105689.
(50) Lee, H.; et al. Electrode Edge Effects and the Failure Mechanism of Lithium-Metal Batteries. *ChemSusChem* **2018**, *11*, 3821−3828.
(51) Fang, C.; et al. Pressure-tailored lithium deposition and dissolution in lithium metal batteries. *Nat. Energy* **2021**, *6*, 987−994.
(52) Levi, M. D.; et al. In Situ Porous Structure Characterization of Electrodes for Energy Storage and Conversion by EQCM-D: a Review. *Electrochim. Acta* **2017**, *232*, 271−284.
(53) Thompson, A. P.; Aktulga, H. M.; Berger, R.; Bolintineanu, D. S.; Brown, W. M.; Crozier, P. S.; in't Veld, P. J.; Kohlmeyer, A.; Moore, S. G.; Nguyen, T. D.; Shan, R.; Stevens, M. J.; Tranchida, J.; Trott, C.; Plimpton, S. J. LAMMPS - a Flexible Simulation Tool for Particle-Based Materials Modeling at the Atomic, Meso, and Continuum Scales. *Comput. Phys. Commun.* **2022**, *271*, 108171.
(54) Jakalian, A.; Bush, B. L.; Jack, D. B.; Bayly, C. I. Fast, Efficient Generation of High-Quality Atomic Charges. AM1-BCC Model: I. Method. *J. Comput. Chem.* **2000**, *21* (2), 132−146.
(55) Gouveia, A. S. L.; Bernardes, C. E. S.; Tomé, L. C.; Lozinskaya, E. I.; Vygodskii, Y. S.; Shaplov, A. S.; Lopes, J. N. C.; Marrucho, I. M. Ionic Liquids with Anions Based on Fluorosulfonyl Derivatives: From Asymmetrical Substitutions to a Consistent Force Field Model. *Phys. Chem. Chem. Phys.* **2017**, *19* (43), 29617−29624.
(56) Heinz, H.; Vaia, R. A.; Farmer, B. L.; Naik, R. R. Accurate Simulation of Surfaces and Interfaces of Face-Centered Cubic Metals Using 12−6 and 9−6 Lennard-Jones Potentials. *J. Phys. Chem. C* **2008**, *112* (44), 17281−17290.
(57) Reed, S. K.; Lanning, O. J.; Madden, P. A. Electrochemical Interface between an Ionic Liquid and a Model Metallic Electrode. *J. Chem. Phys.* **2007**, *126* (8), 084704.
(58) Hockney, R. W. *Computer Simulation Using Particles*; Hilger, 1988.

https://doi.org/10.1021/jacs.5c19365
J. Am. Chem. Soc. 2026, 148, 6365−6378